Materials Science & Engineering A 872 (2023) 144977

Contents lists available at ScienceDirect

Materials Science & Engineering A

journal homepage: www.elsevier.com/locate/msea

Die-cast multicomponent near-eutectic and hypoeutectic Al–Si–Ni–Fe–Mn alloys: Microstructures and mechanical properties

Qing Cai, Ewan Lordan, Shihao Wang, Guangyu Liu, Chamini L. Mendis, Isaac T.H. Chang *, Shouxun Ji

Brunel Centre for Advanced Solidification Technology (BCAST), Brunel University London, Uxbridge, UB8 3PH, UK

ARTICLE INFO

Keywords:
Aluminium alloys
Heat-resistance
Ternary eutectic
Mechanical properties
High pressure die casting

ABSTRACT

Microstructures and mechanical properties of near-eutectic and hypoeutectic Al–Si–Ni–Fe–Mn alloys were studied under as-cast condition. Near-eutectic 78Al15Si4Ni2.5Fe0.5Mn (wt.%) and hypoeutectic 83.6Al11Si3-Ni1.9Fe0.5Mn (wt.%) alloys were processed by high pressure die casting. These two alloys have the same ternary eutectic mixture of α-Al, Si and Al_6(FeNiMn) with a melting point of 567 °C. Primary intermetallic phases of block-like Al_{17}(FeNiMn)$_4$Si and plate-like Al_4(FeNiMn)Si_2 in these two alloys were observed. Precipitates of Si and Ni-contained phase coexist in primary α-Al grains of hypoeutectic alloy. The lattice parameters of Al_6(Fe-NiMn), Al_{17}(FeNiMn)$_4$Si, and Al_4(FeNiMn)Si_2 phases are slightly changed compared with orthorhombic Al_3Ni, orthorhombic $Al_{5.6}Fe_2$ and tetragonal $FeAl_3Si_2$ phases from the database, respectively. These two alloys have excellent mechanical properties at high temperatures. The ultimate tensile strength (UTS) at 300 °C ranges from 135 ± 6 MPa (hypoeutectic alloy) to 157 ± 6 MPa (near-eutectic alloy), which is superior to commercial A383 alloy and some other heat-resistant alloys. Therefore, these near-eutectic and hypoeutectic Al–Si–Ni–Fe–Mn alloys have huge potential for industrial application at elevated temperatures.

1. Introduction

For decades, aluminium alloys have been widely applied in the automotive industry, due to their lightweight [1,2]. Especially, Al–Si cast alloys constitute a major fraction (~85%–90%) of cast aluminium alloys, because of their excellent castability, high corrosion and hot tearing resistance, low thermal expansion and good weldability [3,4]. Generally, near eutectic/hypoeutectic Al–Si based alloys are extensively used in pistons, engine bodies and cylinder heads, which expose to high temperatures [5,6]. With the development of the automotive industry, in particular, the application of new energy such as hydrogen, the performance of the engines needs to be greatly improved. It results in an increase in working temperature and pressure. Thus, it is vital for aluminium alloys to offer the required mechanical properties at high temperatures.

Numerous studies have been carried out for the development of Al–Si based alloys (eutectic/near-eutectic) applied at elevated temperatures, and there are two main approaches, which are particle-reinforced composites and alloying, respectively. First of all, particle-reinforced Al–Si based alloys are effective to improve mechanical properties at elevated temperatures up to 350 °C. For example, Hu et al. developed a near-eutectic Al–Si based alloy with the addition of 1% nano-AlN_p reinforcements and the ultimate tensile strength increased 24.7% at 350 °C [7]. The same approach was also reported by researchers that SiC [8], TiB_2 [9,10] and Al_2O_3 [11] are alternative reinforcements for contributing high-temperature performance of Al–Si based alloys. Secondly, the addition of extra elements into alloys based on a binary Al–Si eutectic system is a traditional method to improve mechanical properties at elevated temperatures. It is mainly focused on precipitation hardening and second phase strengthening. The elements of (0.5–5.5 wt %) Cu and (0.6–1.3 wt%) Mg were commonly employed in Al–Si system [12]. Due to the relatively high solubility of Cu and Mg in α-Al, the alloys after T6 heat treatment are strengthened by θ'-/θ''-Al_2Cu and β′-Mg_9Si_5/β''-Mg_5Si_6 precipitates [13–15]. However, the contributions of these precipitates in strength and creep resistance are very limited, when the alloys are exposed to high temperatures over 250 °C. The rapid coarsening of the precipitates degrades the mechanical properties, induced by the high diffusivity of Cu and Mg in α-Al at elevated temperatures [16]. Although the optimised combination of Cu and Mg in Al–Si based alloys can lead to the formation of Q-$Al_5Cu_2Mg_8Si_6$

* Corresponding author.
E-mail address: isaac.chang@brunel.ac.uk (I.T.H. Chang).

https://doi.org/10.1016/j.msea.2023.144977
Received 24 January 2023; Received in revised form 26 March 2023; Accepted 27 March 2023
Available online 28 March 2023

Table 1
The name and measured composition of the alloys.

Alloy Name	Alloy Composition (wt%)						
	Al	Si	Ni	Fe	Mn	Cu	Zn
A383	Balance	9.52	–	0.82	0.25	1.97	1.24
Alloy A	Balance	15.51	3.80	2.30	0.51	–	–
Alloy B	Balance	11.22	2.81	1.81	0.48	–	–

precipitate, which is more stable than θ'-/θ''-Al_2Cu and β′-Mg_9Si_5/β''-Mg_5Si_6 precipitates at high temperature [17,18], the tensile properties and creep resistance cannot be greatly improved (≥300 °C). Furthermore, the addition of (0.5-3 wt%) Ni and (up to 1.3 wt%) Fe has positive effects on the high-temperature mechanical properties in Al–Si alloys, due to the formation of heat resistance phases such as ϵ-Al_3Ni, δ-Al_3CuNi, γ-Al_7Cu_4Ni, T-Al_9FeNi and β-Al_5FeSi. The 3D network of these heat-resistant phases has a great contribution to mechanical performance at elevated temperatures [19–21]. In addition, transition elements such as Mn, Cr, Mo, and Zr are also important for the strengthing of Al–Si based alloys at high temperatures. Li et al. reported that star-like Mn-contained phases contribute to the increase of strength both at room temperature and high temperature [22]. Gao et al. found that the addition of Zr (2.5 wt%) can form block-like ZrAlSi particles, which can increase ~15% of the ultimate tensile stress and yield stress at elevated temperatures [23].

With respect to alloying method, the selected elements for the development of aluminium alloys applied at high temperatures need to have low diffusivity and solubility in α-Al and are capable of forming heat-resistant phases. There are a few elements including transition elements, and Mn, Ni and Fe are common candidates in Al–Si based alloys. Furthermore, multi-component eutectic aluminium alloys have gained a lot of attention due to their better mechanical or physical performance than their binary counterparts [24–26]. Although ternary Al12.95 wt% Si4.96 wt%Mg [27] and Al11.1 wt%Si4.2 wt%Ni [28,29] eutectic have been investigated which exhibit finer eutectic structure than binary Al–Si eutectic alloy, there is little research on quaternary Al–Si–Ni–Fe eutectic system. Additionally, high-pressure die casting (HPDC) is one of the most popular manufacturing processes of aluminium alloys, which is able to obtain a good surface finish, the complicated shape of castings, and high production efficiency [30]. The popular die-cast alloys for application at elevated temperatures are A380, A383 and A384 alloys [31,32]. Moreover, the alloys need to be solution treated at high temperatures in order to obtain essential precipitates through subsequent ageing. However, die-cast Al–Si alloys are very challenging for T6 heat treatment, mainly due to the increase of porosity defects, surface blistering and dimension instability after solution treatment at high temperatures for a long time [33,34]. Therefore, it is attractive to develop as-cast die-cast alloys for applications at elevated temperatures.

In this study, the multicomponent Al–Si–Ni–Fe eutectic system was employed to design heat-resistant alloys. Minor Mn was selected to improve the anti-solderability. It is also able to facilitate the formation of the fine compact α-AlFeMnSi phase and prevent the formation of needle-like β-AlFeSi phase which is detrimental to mechanical performance [35,36]. The detailed microstructure was characterised by MicroCT, XRD, TEM and SEM. Commerical A383 alloy was employed for the comparison of mechanical properties with newly developed alloys. The

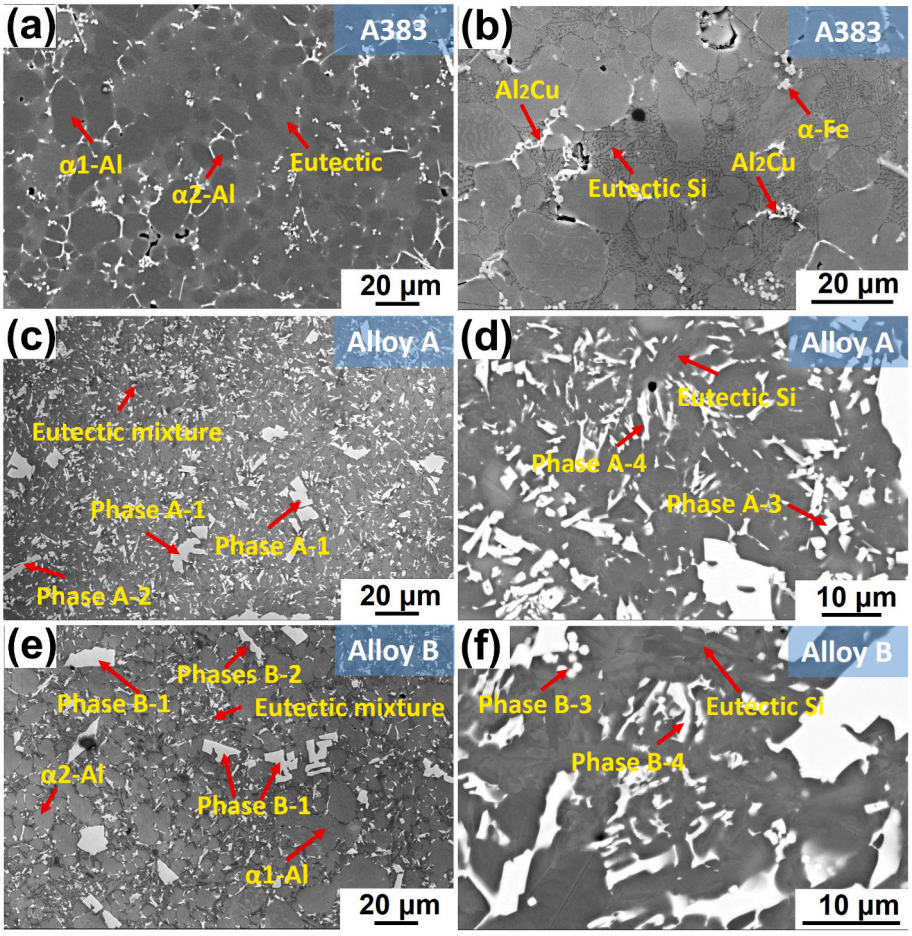

Fig. 1. SEM backscattered images showing the microstructure (a) A383 under low magnification (b) A383 under high magnification (c) Alloy A under low magnification (d) Alloy A under high magnification (e) Alloy B under low magnification (f) Alloy B under high magnification.

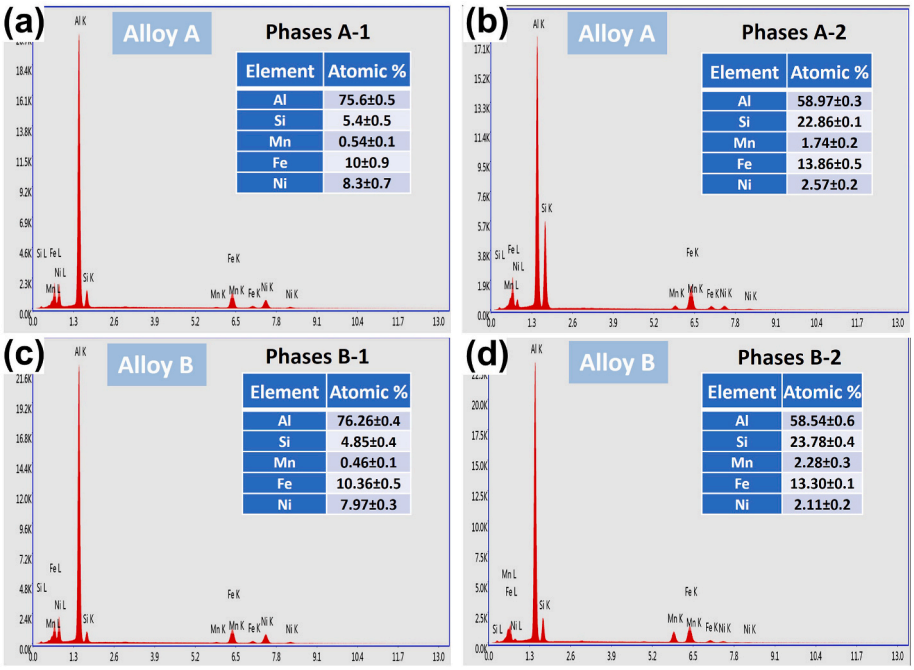

Fig. 2. SEM EDX point analysis of primary intermetallics in Alloy A (a,b) and Alloy B (c,d).

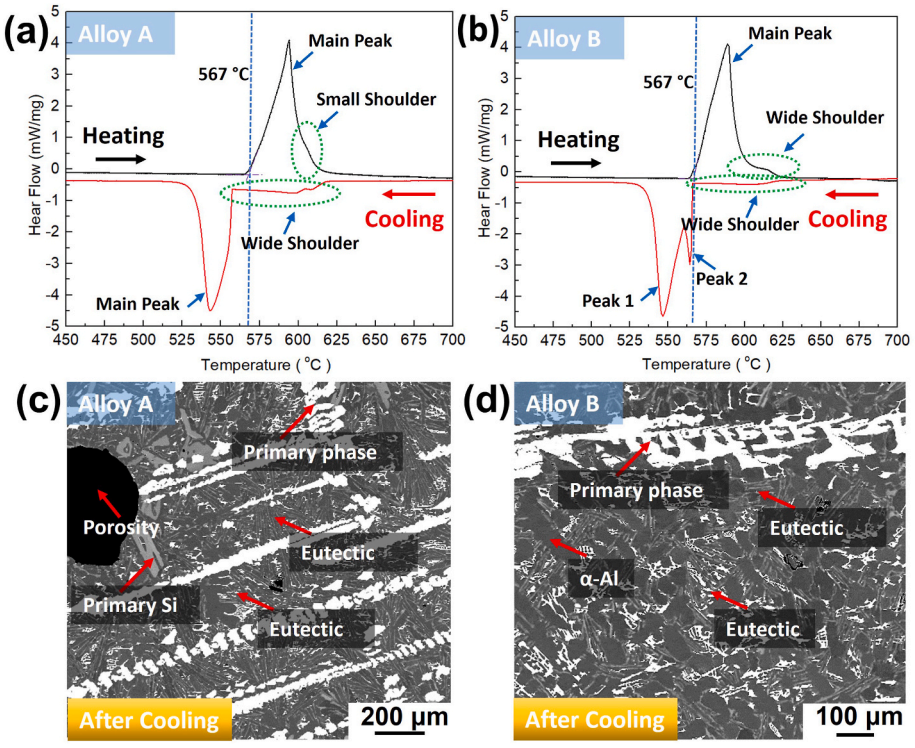

Fig. 3. DSC heating and cooling curves of Alloy A (a) and Alloy B (b); SEM backscattered image showing the microstructure after DSC measurement of Alloy A (c) and Alloy B (d).

relationship between microstructure and mechanical properties at elevated temperatures was established.

2. Experimental

Starting alloys of commerical pure Al, Al50 wt%Si, Al20 wt%Ni, Al10 wt%Fe, pure Cu, pure Zn and Al20 wt%Mn were used for the preparation of the alloys. A 6-kg melt of each alloy was prepared in a clay crucible, which was placed in the electric resistance furnace at 780 °C. After holding for 3 h, the temperature of the furnace was set to 720 °C and pure Zn with an extra 5 wt% weight burning loss was added in A383 alloy. After 15 min, a commerical rotatory degasser with argon gas and a rotation speed of 500 rpm for 10 min was applied for degassing the melt. The melt was covered by granular flux. After 15 min, the melt was poured into the steel mould and a 50 × 80 × 150 ingot was obtained for composition analysis. The ingot was cut and ground with SiC

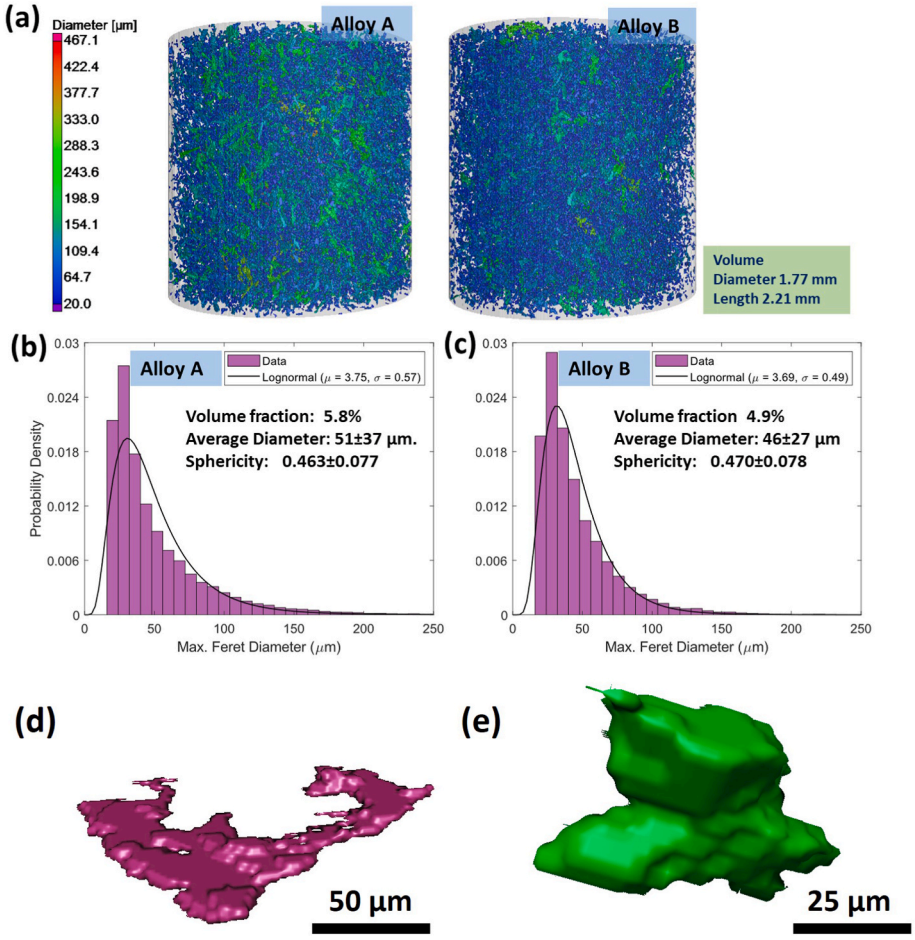

Fig. 4. (a) X-ray micro-CT scans of the volume of Alloy A and Alloy B with size ∅ 1.77 × 2.21 mm showing the primary intermetallic phases; size distribution of primary intermetallic phases in Alloy A (b) and Alloy B (c); typical plate-like morphology of Phase A-2 (d) and block-like morphology of Phase A-1 (e).

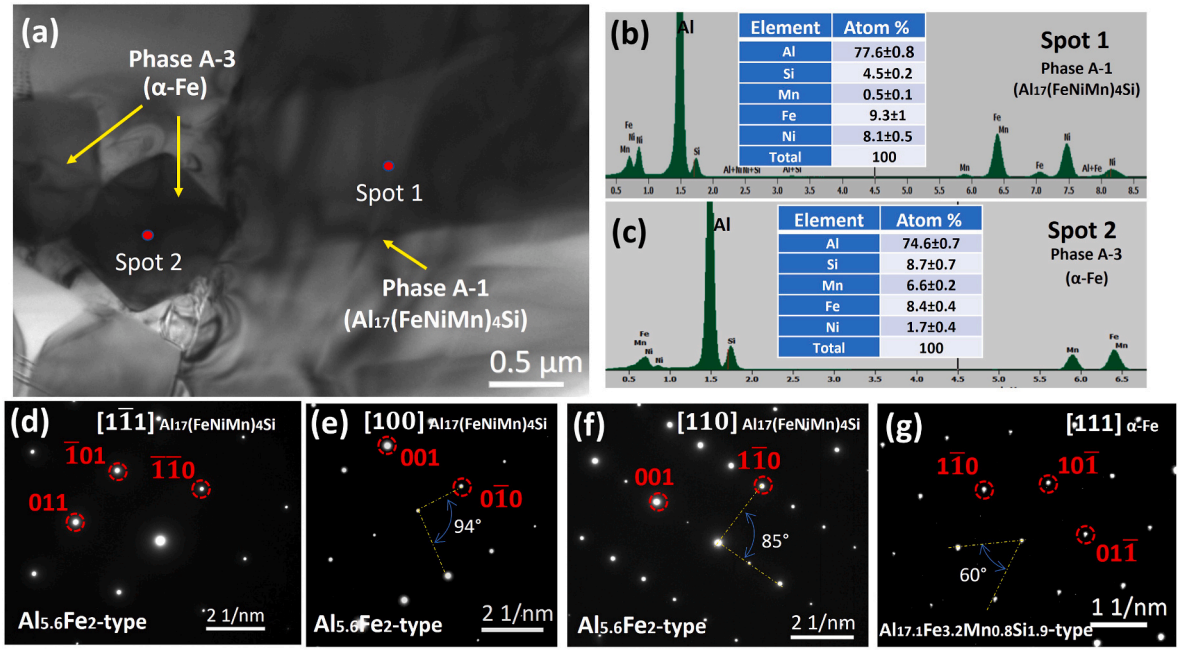

Fig. 5. TEM bright-field image showing the microstructure of Phase A-3 and Phase A-1 (a); TEM EDX point analysis of Phase A-1 (b) and Phase A-3 (c); the SADPs of Phase A-1 (d–f) and Phase A-3 (g).

Table 2
The comparison of lattice parameters between $Al_{5.6}Fe_2$ and $Al_{17}(FeNiMn)_4Si$ (Phase A-1).

Phase name	d-spacing (Å)				Angles between the plans	
	(001)	(0 $\bar{1}$ 0)	(011)	(1 $\bar{1}$ 0)	(00 $\bar{1}$)/(0 $\bar{1}$ 0)	(00 $\bar{1}$)/(1 $\bar{1}$ 0)
$Al_{5.6}Fe_2$	4.218	6.415	3.525	4.917	90°	90°
$Al_{17}(FeNiMn)_4Si$	4.32	6.20	3.39	4.50	94°	85°

sandpaper. The designed composition of hypoeutectic alloy is 83.6Al11Si3Ni1.9Fe0.5Mn (wt.%), and the designed composition of near-eutectic alloy is 78Al15Si4Ni2.5Fe0.5Mn (wt.%). The composition of the alloys was measured with optical mass spectroscopy. The name and the measured composition of the alloys are listed in Table 1.

The melt was dosed and poured into the short sleeve of a 4500 kN HPDC machine. The pouring temperature was controlled at ~700 °C, which was measured by a K-type thermocouple. The standard tensile samples were obtained. The diameter is ∅ 6.35 mm and the gauge length is 50 mm. The dimension of the casting and processing parameters are shown in Fig. S1 (Supplementary Material). The initial injection speed is 0.2 m/s, the theoretical gate speed is 85.7 m/s and the holding pressure is about 320 bar. The die-casting mould was preheated with mineral oil at 200 °C. The samples were subjected to tensile testing using an Instron 5500 mechanical testing machine with a fixed rate of 1 mm/min at room temperature, 200 °C and 300 °C. In terms of tensile testing at 200 °C and 300 °C, the samples were soaked for 40 min before starting the testing programme. The testing data were obtained from at least 6 samples.

The middle part of the tensile testing samples was cut for microstructure characterisation. The microstructure of the alloys was characterised in the central region from the cross-section of the rod. The sample was cold-mounted, ground and polished. After that, a Zeiss Supera 35 FEG SEM equipped with energy dispersive spectroscopy (EDX) was used for the characterisation of the microstructure. The volume fraction of the eutectic mixture was obtained from the SEM backscattered images by Image J software. A Zeiss Auriga cross beam 420 SEM-FIB (focused ion beam) was used for the preparation of transmission electron microscopy (TEM) samples. The samples were milled to a thickness of about 80 nm and attached to the Cu grid. A JEOL 2100F TEM was used to study the eutectic region and primary phases. The cooling and heating curves of the alloys were obtained by a Netzsch 404F1 differential scanning calorimeter (DSC) at a heating/cooling rate of 10 K/min and a dynamic flow of 50 ml/min of argon gas. The X-ray diffraction (XRD) sample was prepared from the cross-section of the ∅ 6.35 tensile testing rod. A Bruker D8 Advance X-ray diffractometer with Cu X-Ray radiation and Ni filter operated at a voltage of 40 kV and a current of 40 mA was used to generate X-ray line profiles on each sample for phase identification. 3D morphology and volume fraction of primary phases in the alloys were characterised by Micro-CT (Zeiss Xradia 410 Versa X-ray). A Carbolite electric furnace was used for heat treatment. The furnace was preheated to 300 °C and held for 1 h before putting samples inside. The samples were cut from the Φ6.35 tensile testing rod with a thickness of 2.5 mm. Micro-CT was applied for the characterisation of pores in the same sample of each alloy before and after heat treatment.

3. Results

3.1. SEM results

The backscattered SEM images of Fig. 1 (a) and (b) show the microstructure of A383 alloy. There is a dual-size distribution of α-Al grains, labelled as α_1-Al and α_2-Al. The α_1-Al and α_2-Al grains have

Table 3
The comparison of lattice parameters between $FeAl_3Si_2$ and $Al_4(FeNiMn)Si_2$ (Phase A-2).

Phase name	d-spacing (Å)				Angles between the plans		
	($\bar{2}$ 00)	(002)	(01 $\bar{1}$)	(1 $\bar{1}$ 0)	(1 $\bar{1}$ 0)/(00$\bar{2}$)	(200)/(01 $\bar{1}$)	(00 $\bar{2}$)/(2 $\bar{1}$ 0)
$FeAl_3Si_2$	3.030	4.762	5.114	4.286	90°	90°	90°
$Al_4(FeNiMn)Si_2$	3.20	4.69	5.03	4.22	88°	85°	89°

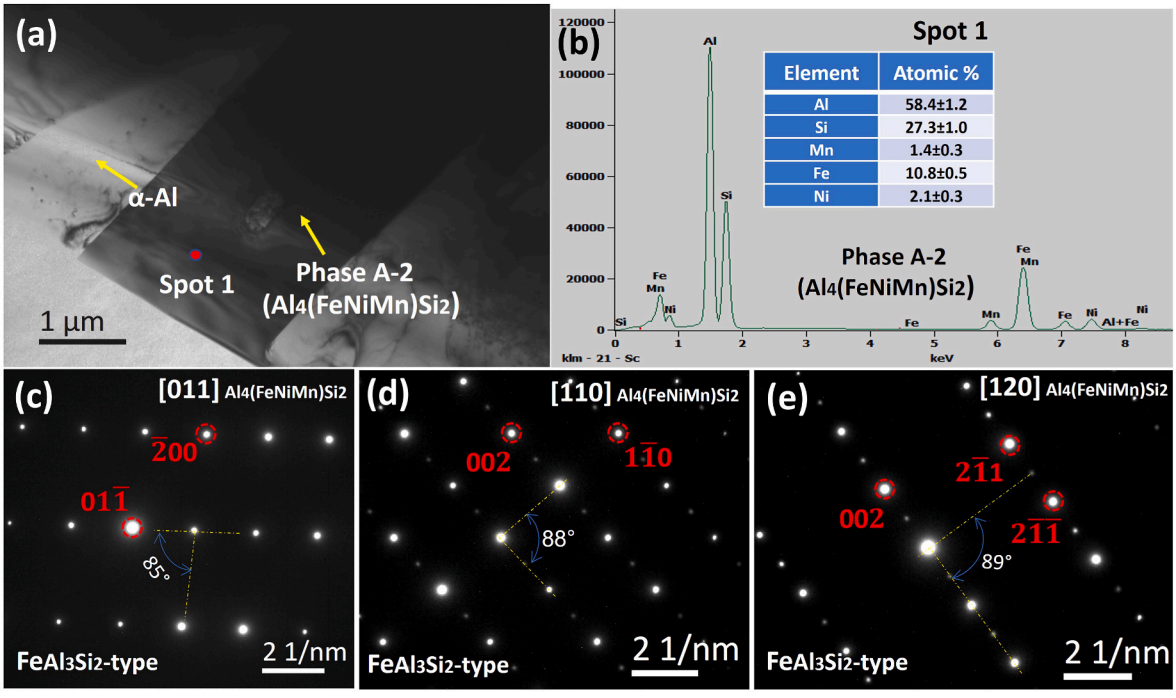

Fig. 6. TEM bright-field image showing the microstructure of Phase A-2 (a); TEM EDX point analysis of Phase A-2 (b); the SADPs of Phase A-2 (c–e).

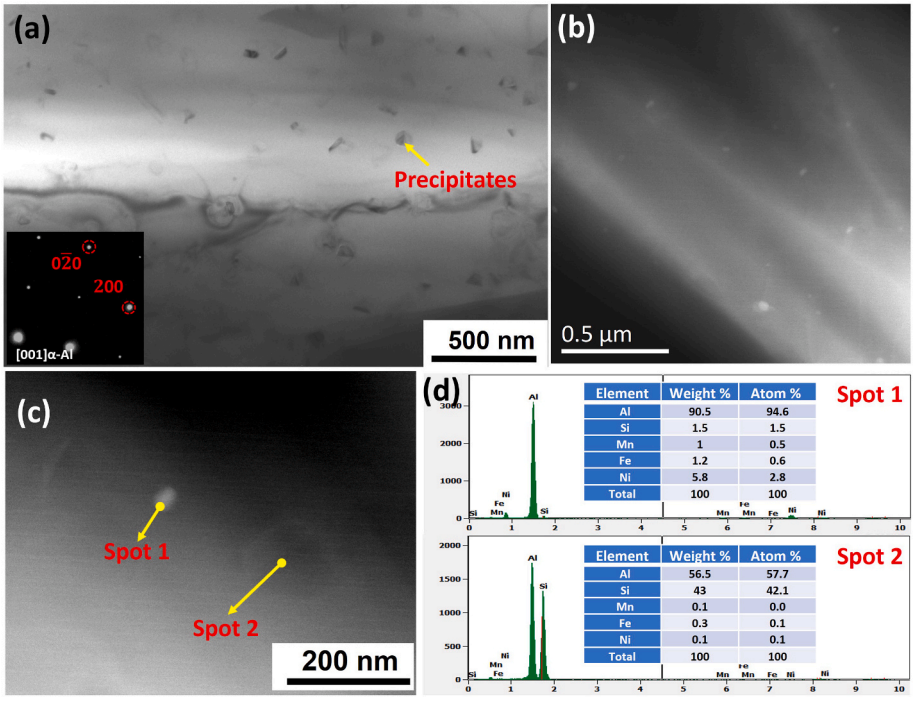

Fig. 7. (a) TEM bright-field image of α-Al grain from Alloy B with inserted SADP of α-Al (b) HAADF STEM image under low magnification (c) high-magnified HAADF STEM image showing the precipitates (d) EDX point analysis of Spot 1 and Spot 2 from (c).

average sizes of 20 ± 5 μm and 8 ± 4 μm. It corresponds to the two-step solidification in the short sleeve and die cavity, respectively [37]. From Fig. 1 (b), the eutectic Si, eutectic Al_2Cu and fine compact α-AlFeMnSi phases are distributed at the interdendritic regions. Fig. 1 (c) shows the microstructure of Alloy A. The microstructure consists of primary intermetallic phases and a eutectic mixture. There are only two types of primary intermetallic phases based on morphology. They are plate-like and block-like, labelled as Phase A-2 and Phase A-1, respectively. High-magnification image of the microstructure is shown in Fig. 1 (d). There are Si and plate-like phase (labelled as Phase A-4) in the eutectic mixture, and some compact intermetallics (labelled as Phase A-3) are near the eutectic region. From Fig. 1 (e), it can be seen that there are some primary α_1-Al and α_2-Al grains in Alloy B, with average sizes of 22 ± 5 μm and 10 ± 4 μm respectively. The area fraction of α-Al is about 40% which was obtained by image analysis. The plate-like and block-like intermetallics in Alloy B are similar to those in Alloy A. They are labelled as Phase B-2 and Phase B-1. Fig. 1 (f) shows a high-magnification image of microstructure in the eutectic region. Si and plate-like phases (labelled as Phase B-4) were found in the eutectic region, and fine compact intermetallics (labelled as Phase B-3) distribute near the eutectic region.

In order to further confirm the types of primary intermetallic phases in these two alloys, SEM EDX point analysis was carried out in each alloy, and at least 50 points of EDX analysis were obtained in each alloy. The SEM EDX results are shown in Fig. 2. From the SEM EDX results, it can be confirmed that there are mainly two types of primary intermetallics both in Alloy A and Alloy B. The block-like Phase A-1 and Phase B-1 are the same phases, and the plate-like Phase A-2 and Phase B-2 are also the same phases. Based on the composition, the plate-like phase has a much higher content of Si and a lower content of Ni compared with the composition of the block-like phase. The dissolution of Mn takes place in the formation of these primary intermetallic phases.

3.2. DSC results

Fig. 3 (a) shows the DSC heating and cooling curves of Alloy A. From the heating curve, It can be noticed that there are a main peak and a small shoulder in the heating curve from low to high temperature. Based on the SEM results in Fig. 1 (c), it can be induced that the main peak corresponds to the melting of the eutectic mixture and the small shoulder corresponds to the melting of primary intermetallic phases. The heating curve of Alloy B is shown in Fig. 3 (b). One main peak and a wide shoulder were found in the curve. Based on the SEM results in Fig. 1 (e), the main peak corresponds to the melting of the eutectic mixture. The wide shoulder corresponds to the melting of intermetallic phases and α-Al grains. Both Alloy A and Alloy B have the same melting temperature of 567 °C. In addition, it can be observed that there is one peak with a wide shoulder in the cooling curve of Alloy A shown in Fig. 3 (a). The microstructure of the sample after DSC measurement is shown in Fig. 3 (c). The microstructure consists of primary Si, dendritic intermetallic phases and a eutectic mixture. Combined with the cooling curve, the main peak corresponds to the solidification eutectic mixture at low temperatures and the wide shoulder corresponds to the formation of Si and primary intermetallic phases at high temperatures. The DSC cooling curve and the microstructure after DSC measurement of Alloy B are shown in Fig. 3 (b) and Fig. 3 (d), respectively. There are two peaks and a shoulder in the cooling curve of Alloy B. The two peaks from low temperature to high temperature correspond to the formation of the eutectic mixture and α-Al, and the wide shoulder corresponds to the formation of primary intermetallic phases.

3.3. Micro-CT results

Fig. 4 (a) shows the X-ray Micro-CT scans of the volume with a size of ∅ 1.77 × 2.21 mm in Alloy A (left) and Alloy B (right). The average size distributions of Alloy A and Alloy B are shown in Fig. 4 (b) and (c), respectively. The volume fraction of the primary intermetallics in Alloy A is 5.8%, which is slightly higher than that in Alloy B (4.9%). There is a wide size distribution of primary intermetallic phases in Alloy A and Alloy B. A very small number of intermetallic phases has a size of over 200 μm, which is because of the dual-step solidification under HPDC [36]. Alloy A has a coarser size of primary intermetallic phases (51 ± 37 μm) than that (46 ± 27 μm) in Alloy B. However, the average sphericity in these two alloys is very close. It indicates the morphology of the

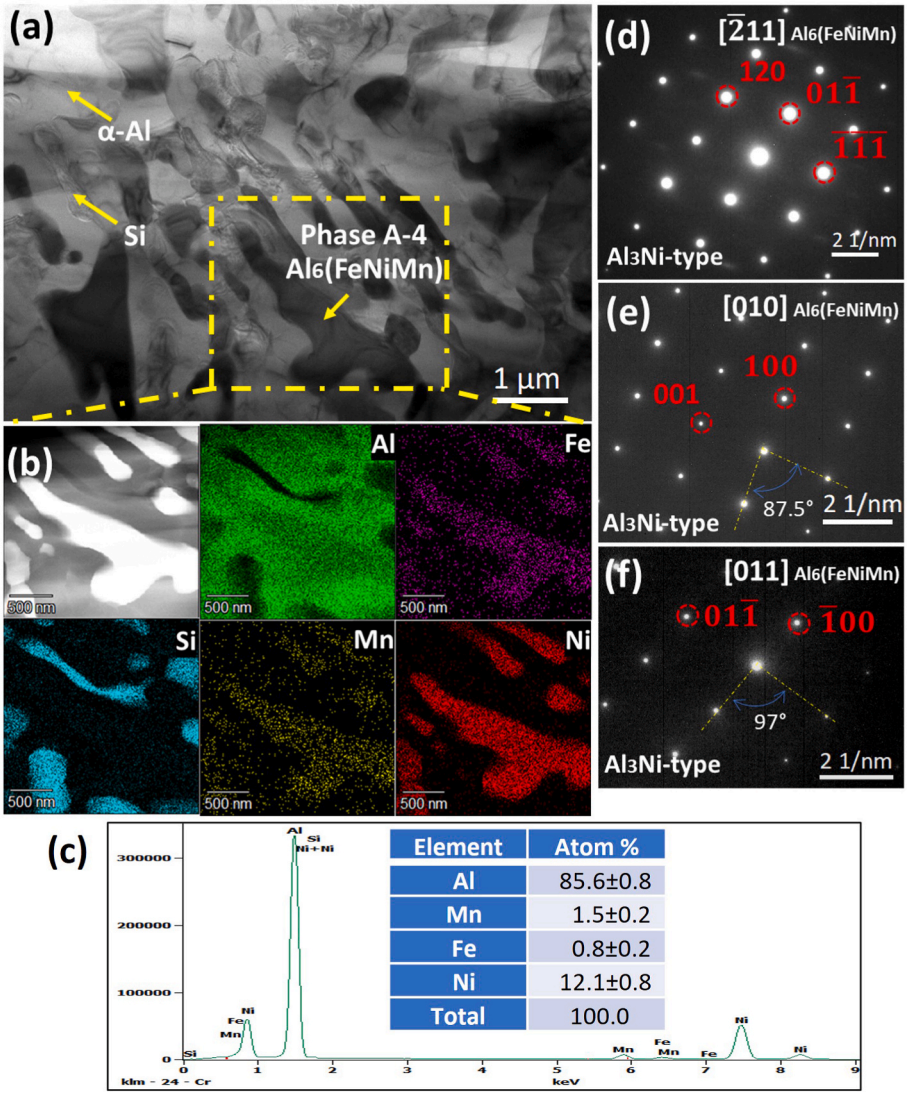

Fig. 8. (a) TEM bright-field image of the eutectic region in Alloy A; (b) HAADF STEM image and EDX mapping of the selected region in (a); (c) TEM EDX analysis of Phase A-4; (d–f) the SADPs of Phase A-4.

Table 4
The comparison of lattice parameters between Al_3Ni and $Al_6(FeNiMn)$ (Phase A-4).

Phase name	d-spacing (Å)				Angles between the plans		
	(001)	(100)	(01 $\bar{1}$)	($\bar{1}\bar{1}\bar{1}$)	(001)/(100)	(01 $\bar{1}$)/($\bar{1}$ 00)	(01 $\bar{1}$)/($\bar{1}\bar{1}\bar{1}$)
Al_3Ni	4.801	6.598	4.020	3.433	90°	90°	69.9°
$Al_6(FeNiMn)$	5.04	6.21	4.27	3.57	87.5	97	69.0°

primary intermetallics in these two alloys is quite similar. In addition, the typical morphologies of Phase A-2 and Phase A-1 are shown in Fig. 4 (d) and (e), respectively. It is confirmed that Phase A-2 shows irregular plate-like morphology, while Phase A-1 shows block-like morphology.

3.4. TEM results

Fig. 5 (a) shows the TEM bright field image of primary Phase A-3 and Phase A-1. The average compositions measured by TEM EDX point analysis of Phase A-1 and Phase A-3 are shown in Fig. 5 (b) and 5 (c), respectively. The compositions are close to that measured under SEM EDX point analysis shown in Fig. 2. Based on the composition, the structure formula of Phase A-1 is close to $Al_{17}(FeNiMn)_4Si$, and corresponding selected area diffraction patterns (SADPs) are shown in Fig. 5 (d–f). The SADPs were identified based on orthorhombic $Al_{5.6}Fe_2$ phase (a = 7.656 Å, b = 6.415 Å, c = 4.218 Å and α = β = λ = 90°) [38]. However, there is a slight lattice distortion of $Al_{17}(FeNiMn)_4Si$ (Phase A-1) compared with $Al_{5.6}Fe_2$ phase. The differences in the lattice parameters are listed in Table 2. The d-spacings are slightly different between these two phases. It can be also found that the angles of (00 $\bar{1}$)/(0 $\bar{1}$ 0) and (00$\bar{1}$)/(1 $\bar{1}$ 0) are not 90°, indicating it is not orthorhombic. In addition, Phase A-3 was identified to be $Al_{17.1}Fe_{3.2}Mn_{0.8}Si_{1.9}$-type phase from the TEM diffraction pattern in Fig. 5 (g) [39]. The lattice parameters of Phase A-3 including d-spacing and angle are almost the same as the $Al_{17.1}Fe_{3.2}Mn_{0.8}Si_{1.9}$ phase, indicating that there is no distortion in the crystal. However, the composition of Phase A-3 shown in Fig. 5 (c) is different from $Al_{17.1}Fe_{3.2}Mn_{0.8}Si_{1.9}$ phase, and the structure formula of

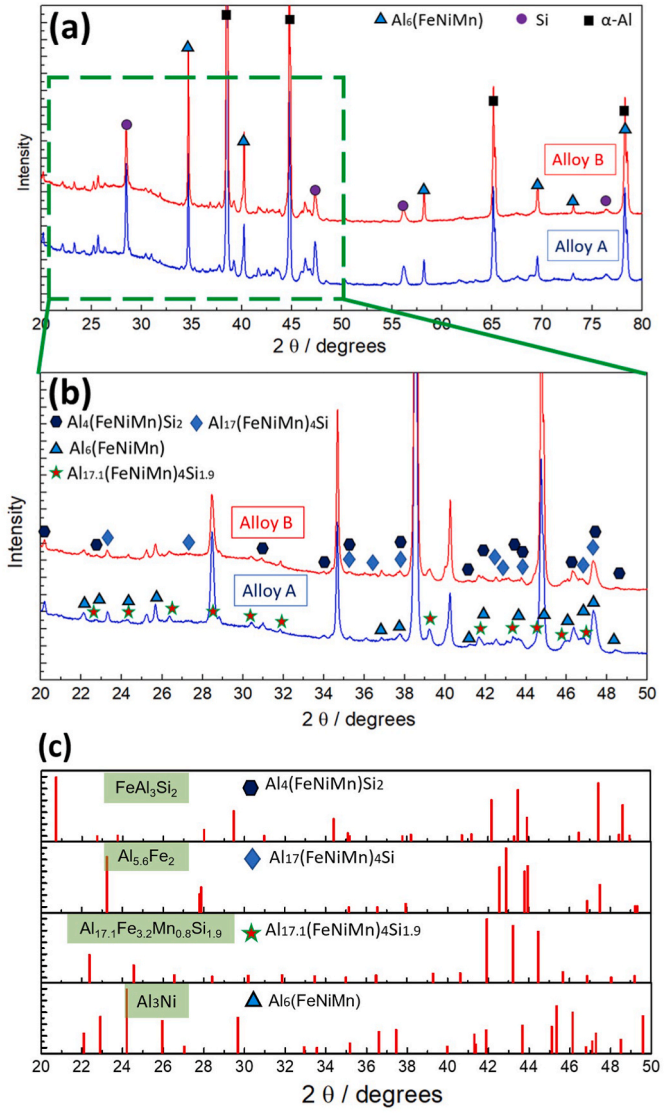

Fig. 9. XRD patterns of Alloy A and Alloy B with 2 θ angles from 20° to 80° (a) and from 20° to 50° (b); (c) the power XRD patterns of $FeAl_3Si_2$, $Al_{5.6}Fe_2$, $Al_{17.1}Fe_{3.2}Mn_{0.8}Si_{1.9}$, and Al_3Ni phases from the database with 2 θ angles from 20° to 50°.

Phase A-3 is close to $Al_{17.1}(FeNiMn)_4Si_{1.9}$. It can be found that only the minor substitution of Ni in Fe or Mn occurs, which is not able to lead to some distortion of the crystal. Hence, the lattice parameters of $Al_{17.1}(FeNiMn)_4Si_{1.9}$ are almost the same as $Al_{17.1}Fe_{3.2}Mn_{0.8}Si_{1.9}$ which is from the database.

Fig. 6 (a) shows TEM bright-filed image of Phase A-2. The corresponding TEM EDX point analysis of the composition of Phase A-2 is shown in Fig. 6 (b). The structure formula of Phase A-2 is close to $Al_4(FeNiMn)Si_2$. The SADPs in Fig. 6(c–e) of Phase A-2 were identified based on the tetragonal $FeAl_3Si_2$ phase [40]. Compared with the tetragonal $FeAl_3Si_2$ phase (a = b = 6.061 Å, c = 9.525 Å and α = β = λ = 90°), Phase A-2 has a lattice distortion. The comparison of the lattice parameters between the $FeAl_3Si_2$ phase and Phase A-2 is shown in Table 3. The d-spacings are slightly different between these two phases. It can be also found that the angles of $(1\ \bar{1}\ 0)/(00\bar{2})$, $(200)/(01\ \bar{1})$ and $(00\ \bar{2})/(2\ \bar{1}\ 0)$ are not 90°, and the crystal structure of $Al_4(FeNiMn)Si_2$ is not tetragonal.

TEM bright-field image of the precipitates in α-Al from Alloy B is shown in Fig. 7 (a). There are a large number of precipitates inside α-Al grains from Alloy B.

Fig. 7 (b) shows HAADF STEM image under low magnification and some bright precipitates with a size below 60 nm are inside the α-Al grains. From the high-magnified HAADF STEM image (Fig. 7 (c)), there are a dark coarse granular precipitate and a bright fine granular precipitate. EDX point analysis (Fig. 7 (d)) confirmed that the dark precipitate is Si phase and the bright precipitate is the Ni-contained phase with a little Fe, Mn and Si.

Fig. 8 (a) shows the TEM bright-field image of the microstructure of the eutectic region in Alloy A. There are fibrous Si phases and plate-like Phase A-4 inside the eutectic region, corresponding to the SEM results in Fig. 1 (d). Fig. 8 (b) shows HAADF STEM image and EDX mapping of the selected region in Fig. 8 (a). It is further confirmed that there are three eutectic phases (α-Al + Si + Phase A-4) in this region, and Phase A-4 has four elements, which are Al, Mn, Fe and Ni. The average composition of Phase A-4 was obtained by TEM EDX analysis, as shown in Fig. 8 (c). The structure formula is close to $Al_6(FeNiMn)$. The SADPs of Phase A-4 shown in Fig. 8(d–f) were identified based on the orthorhombic Al_3Ni phase (a = 6.598 Å, b = 7.352 Å, c = 4.801 Å and α = β = λ = 90°). Compared with the orthorhombic Al_3Ni phase, there is a crystal distortion in Phase A-4. The comparison of lattice parameters between Al_3Ni phase and Phase A-4 is shown in Table 4. There are slight differences in the lattice parameters and the angle between (001) and (100) in Phase A-4 is 87.5°, indicating the crystal structure is not orthorhombic. The TEM result of the eutectic region in Alloy B is shown in Fig. S2 (Supplementary Material). The microstructures of the eutectic region between Alloy A and Alloy B are the same, and they are both ternary eutectic reactions consisting of α-Al, Si and $Al_6(FeNiMn)$ phases.

3.5. XRD results

Fig. 9 (a) shows the XRD patterns of Alloy A and Alloy B with 2θ angles from 20° to 80°. The reference XRD patterns of corresponding phases from the database are shown in Fig. 9 (c). The XRD patterns of these two alloys are similar, which indicates that these two alloys have the same phases. The peaks having relatively high intensities were identified to be Si, α-Al and $Al_6(FeNiMn)$ phases, indicating their high volume fractions. Fig. 9 (b) shows XRD patterns with 2θ angles from 20° to 50°. The small peaks were also identified, which correspond to primary intermetallic phases and the eutectic $Al_6(FeNiMn)$ phase from TEM results.

3.6. Mechanical properties

Fig. 10(a–c) shows the typical tensile testing curves of A383, Alloy A and Alloy B at room temperature, 200 °C and 300 °C, respectively. The statistical mean tensile properties of A383, Alloy A and Alloy B are shown in Fig. 10(d–f). A383 has the highest UTS of 305 ± 7 MPa and EL of 5.2 ± 0.7%, as well as the lowest YS of 140 ± 3 MPa at room temperature. Alloy A has the highest YS of 202 ± 6 MPa and the lowest EL of 0.95 ± 0.2% at room temperature. There is a decrement in UTS in Alloy A and Alloy B from room temperature to 300 °C, which is from 273 ± 10 MPa to 157 ± 6 MPa in Alloy A, and from 283 ± 8 MPa to 135 ± 6 MPa in Alloy B. The UTS in A383 drops dramatically from room temperature to 300 °C, which is from 305 ± 7 MPa to 75 ± 4 MPa. The YS shows a similar trend in these three alloys from room temperature to 300 °C. The YS in A383, Alloy A and Alloy B at 300 °C are 68 ± 3 MPa, 149 ± 3 MPa, and 127 ± 4 MPa, respectively. The developed alloys have much higher YS at 300 °C than A383. The EL in these three alloys increases greatly from room temperature to 300 °C. Especially, EL in A383 increases from 5.2 ± 0.7% at room temperature to 21 ± 2.5% at 300 °C. The EL of Alloy A and Alloy B at 300 °C are 6.5 ± 0.8% and 10 ± 1.1%, respectively.

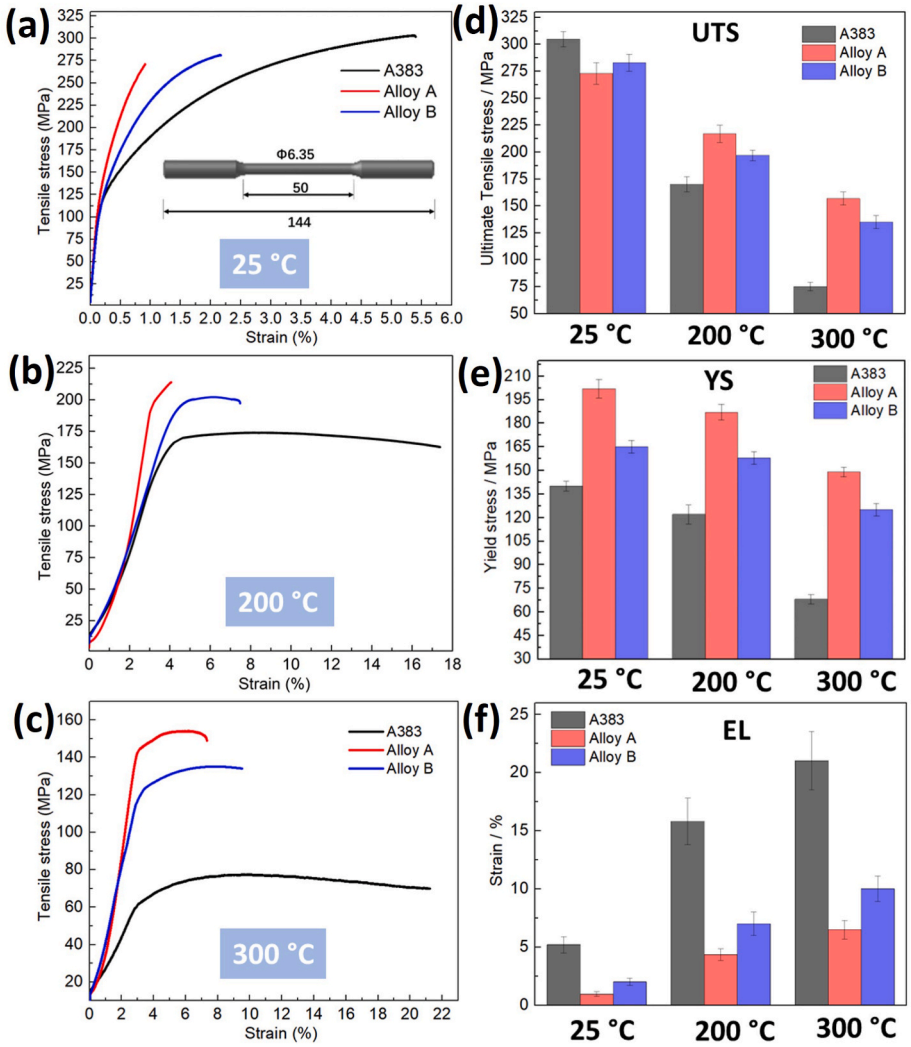

Fig. 10. Typical tensile testing curves of A383, Alloy A and Alloy B at room temperature (a), 200 °C (b) and 300 °C (c); statistical mean tensile properties of A383, Alloy A and Alloy B (d) ultimate tensile strength (UTS) (e) yield strength (YS) (f) elongation (EL).

4. Discussion

4.1. Microstructural evolution

Fig. 11 shows SEM EDX mapping of the microstructure in the eutectic region of Alloy B after DSC measurement. The element distribution of Al, Si, Mn, Fe and Ni is displayed, and it can be found that there are four phases in this eutectic mixture, which are (AlNi) phase, Si, α-Al and (AlNiFeMn) phase. (AlNi) phase is marked by the red dashed circles, (AlNiFeMn) phase is marked by the cyan-blue dashed circles and Si is marked by the orange dashed circles. (AlNi) phase shows polygonal morphology, and (AlNiFeMn) phase shows Chinese-script morphology. The cooling rate is 10 K/min, and the solidification is close to an equilibrium state. It can be induced that under a near-equilibrium state, the eutectic mixture in Alloy B is a quaternary eutectic reaction. Fig. 11 (b) and (c) show the SEM EDX point analysis of Spot 1 and Spot 2, which corresponds to the (AlNi) and (AlFeNiMn) phases in Fig. 11 (a), respectively. The (AlNi) phase is Al_3Ni, and the structure formula of (AlFeNiMn) phase is close to $Al_9(FeNiMn)_2$. The results of eutectic microstructure obtained after DSC measurement in Alloy A is similar, which is not shown here.

It is reported that there is an invariant quaternary eutectic reaction at ~556 °C in the Al–Fe–Ni–Si system, which is Liquid→α-Al + Si+ϵ-Al_3Ni + T-Al_9FeNi [12]. T-Al_9FeNi has a monoclinic crystal structure, and the substitution of Ni and Fe in T-Al_9FeNi phase leading to different ratios of Ni/Fe can usually be found [41,42]. In the current work, there is a quaternary eutectic reaction of Liquid→α-Al + Si + Al_3Ni + $Al_9(FeNiMn)_2$ in the Al–Si–Ni–Fe–Mn system under near-equilibrium conditions. It can be induced that $Al_9(FeNiMn)_2$ is T-Al_9FeNi type phase with the dissolution of Mn and a certain ratio of Ni/Fe. However, under rapid solidification (HPDC), it becomes a ternary eutectic reaction of Liquid→α-Al + Si + Al_6(FeNiMn) at 567 °C. The structure of materials depends on Gibbs free energy at a given temperature, which can be described as $\Delta G = \Delta H - T\Delta S$. Here, ΔG is Gibbs free energy and T is temperature. ΔH is enthalpy of mixing, which is mainly determined by the interaction energies of the component atoms and molecules. ΔS is entropy of mixing, which is mainly determined by the configurational entropy of mixing the different component atoms or molecules. In high entropy alloys, entropy plays a dominant role in Gibbs free energy. Thus, the formation single solid solution phase can be facilitated, while the formation of intermetallic phases is suppressed [43]. Here, because of the many components involved in eutectic solidification, the entropy of mixing (ΔS) can be increased, but the enthalpy of mixing (ΔH) is still dominant resulting in the formation of intermetallic phases [44]. A relatively high entropy of mixing (ΔS) at high temperatures is able to facilitate the formation of non-stoichiometry intermetallic compounds, and additional elements are accommodated based on binary or ternary intermetallic structures [45]. Due to the different atomic sizes and

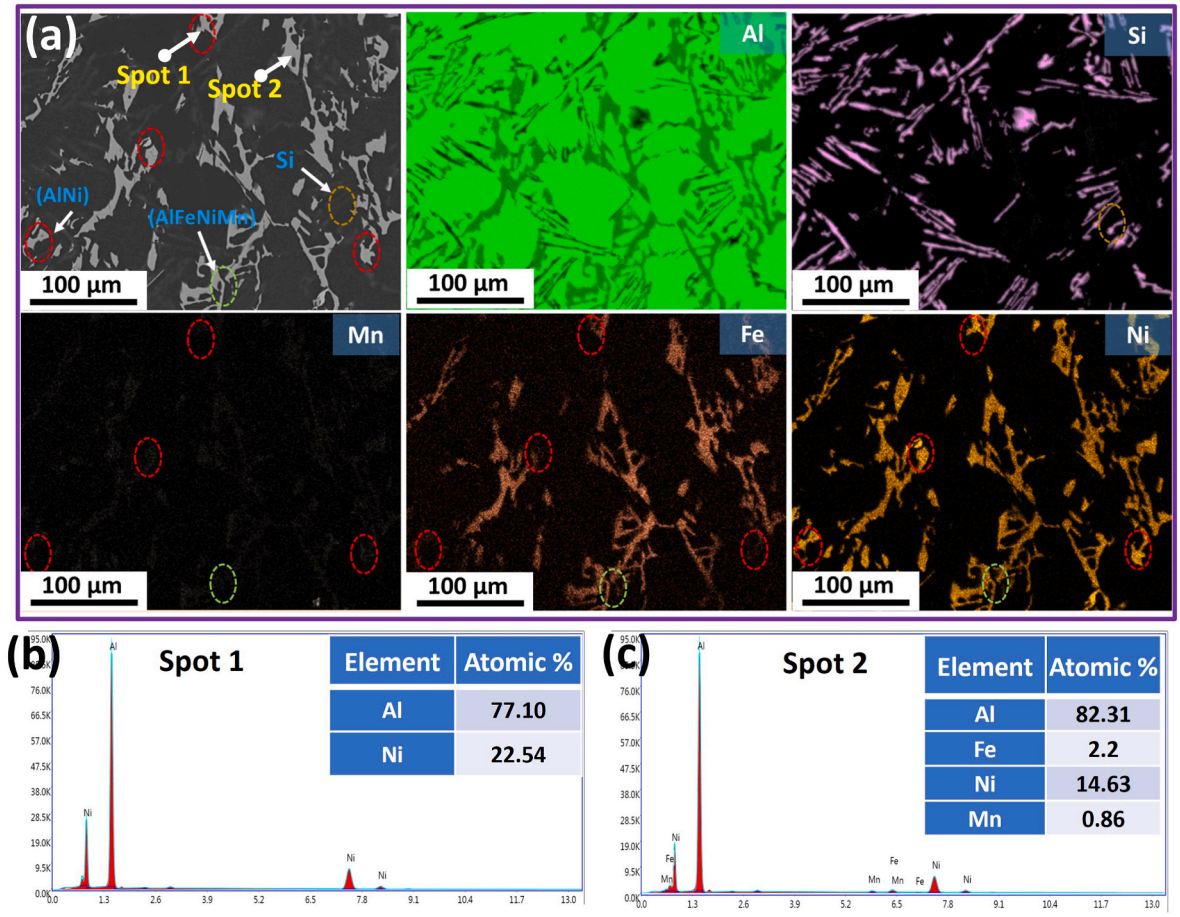

Fig. 11. (a) SEM EDX mapping of the eutectic mixture in Alloy B after DSC measurement (10 K/min); SEM EDX point analysis of Spot 1 (b) and Spot 2 (c).

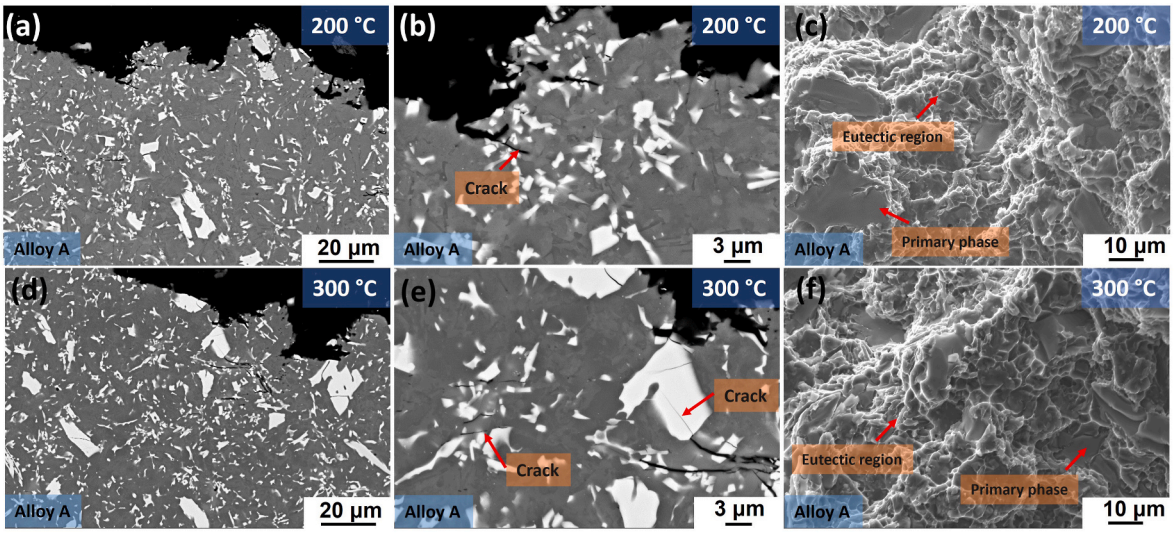

Fig. 12. SEM backscattered images showing the fracture surface of Alloy A after tensile testing at 200 °C (a–c) and 300 °C (d–f).

interactions among the additional components, lattice distortion can be found compared with the binary or ternary standard intermetallic structure. In addition, it can be found that with the decreased cooling rates the eutectic solidification transformed from a ternary reaction to a quaternary reaction with two types of intermetallic phases. The phenomenon is similar to high-entropy alloys at different cooling rates [46, 47]. It is reported that under a very slow cooling rate or high-temperature annealing, phase decomposition takes place in high entropy alloys, and some intermetallic phases form rather than one or two solid solution phases. Here, at a slower cooling rate, the thermodynamic entropy loses its contribution. The diffusion has sufficient time, leading to the formation of extra intermetallic phases. The supersaturated phases are decomposed and disappeared. As a result, the eutectic transforms from a ternary reaction to a quaternary reaction.

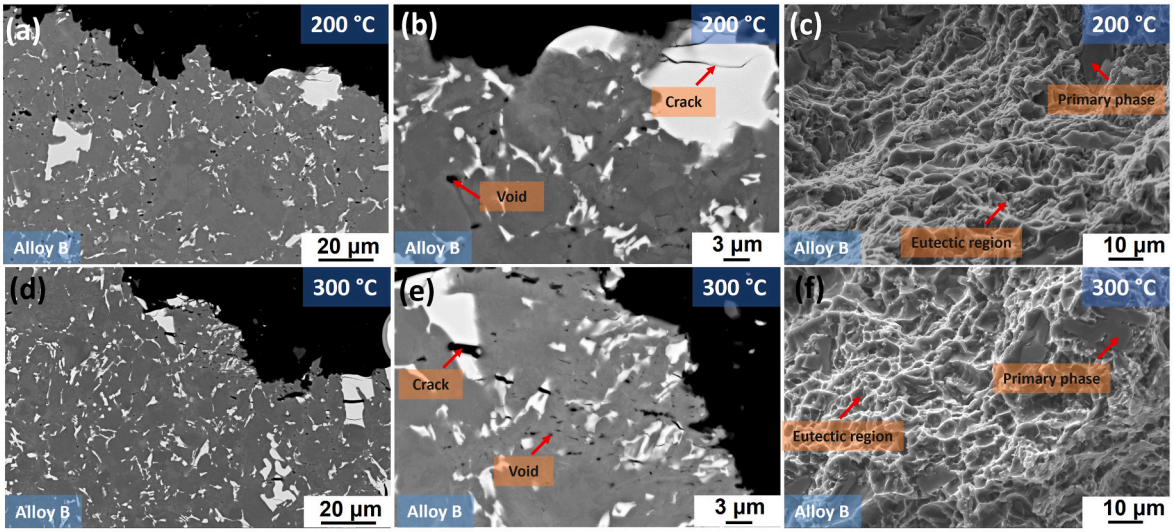

Fig. 13. SEM backscattered images showing the fracture surface of Alloy B after tensile testing at 200 °C (a–c) and 300 °C (d–f).

Table 5
Mechanical properties of the heat-resistant alloys at room and elevated temperatures.

Alloys (Condition)		Temperature/ °C	YS/ MPa	UTS/ MPa	EL/%
Al12Si4Cu2Ni0.8 Mg (T6) [55]		25	–	390	1
		200	–	325	4
		300	–	140	4
Al12Si4Cu2Ni0.8Mg0.2Nd (As-cast) [56]		25	196.6	240.5	0.89
		200	173.6	192.7	1.31
		300	101.9	118.5	4.81
Al12Si4Cu2Ni0.8Mg0.2Gd (T6) [55]		25	–	425	1
		200	–	356	5
		300	–	153	5
Al6.72Si6Cu0.6Mn0.6Fe0.13 Mg (T6) [57]		25	~210	~250	~2.5
		300	~125	~145	~4
AA2618 (T6) [58]		300	95	100	20
Al13Si0.6Fe3Cu0.6Mn0.15Ti (T6) [6]		25	210	285	2.7
		300	125	138	8.5
Al13Si0.6Fe5Cu0.6Mn0.15Ti (T6) [6]		25	280	336	0.82
		300	130	144	7.2
A383 (As-cast)		25	140 ± 3	305 ± 7	5.2 ± 0.7
		200	122 ± 6	170 ± 7	15.8 ± 2
		300	68 ± 3	75 ± 4	21 ± 2.5
Current Work	**Alloy A (As-cast)**	25	202 ± 6	273 ± 10	0.95 ± 0.2
		200	187 ± 5	217 ± 8	4.35 ± 0.5
		300	149 ± 3	157 ± 6	6.5 ± 0.8
	Alloy B (As-cast)	25	165 ± 4	283 ± 8	2 ± 0.3
		200	156 ± 4	197 ± 5	7 ± 1
		300	128 ± 4	135 ± 6	10 ± 1.1

In addition, there are three types of multicomponent primary intermetallic phases, and one is a well-known α-AlFeMnSi type phase. A similar phenomenon was reported by some researchers [42,48,49]. Intermetallic phases of Al(TM)Si with supersaturated elements (TM represents transition elements such as Fe, Mn, Ni, Cr, V, Cu) can usually be found in multicomponent Al–Si based piston alloys instead of many binary or ternary intermetallic phases. In addition, based on the TEM characterisation in the current work, the crystal structure of these primary intermetallics can be regarded as the distortion of basic binary or ternary orthorhombic and tetragonal phases. The distortion may originate from the interstitial or substitution of different atoms in the orthorhombic and tetragonal phases. Simialr phenomenon is also reported by Jo et al. [50] and it was found that the primary $(Al,Si)_3(Zr,Ni,Fe)$ phase can be regarded as Al_3Zr-D023 crystal (tetragonal, *I*4/mmm (139)) with lattice distortion. The formation of multicomponent supersaturated intermetallic phases is able to reduce the enthalpies of the system compared with the formation of numerous binary or ternary intermetallic phases. Thus, it is very common that multicomponent intermetallic phases can usually be found instead of many types of binary or ternary intermetallic phases in multicomponent alloys.

4.2. *Relationship between microstructure and mechanical properties*

Fig. 12 shows the fracture surface of Alloy A after tensile testing at 200 °C and 300 °C. The microstructures of Alloy A after tensile testing at 200 °C and 300 °C are similar. It can be found that the facture surface consists of a mixture of dimples and cleavage. The cleavage corresponds to primary intermetallic phases, while the dimples correspond to the eutectic mixture. The cracks can be observed both at $Al_6(FeNiMn)$ phase and primary intermetallic phases, indicating the crack initiation and propagation along these intermetallic phases. It can be induced that during the tension at elevated temperatures, these intermetallic phases bear the load and prohibit the deformation of α-Al grains which becomes very soft at elevated temperatures. No cracks can be found inside the brittle Si phase, which may result from its fine microstructure. The microstructure of the fracture surface in Alloy B after tensile testing at 200 °C and 300 °C is shown in Fig. 13. The fracture surface also consists of dimples and cleavage. Apart from the cracks in the intermetallic phases, there are numerous microvoids inside the eutectic region which reflects its high elongation. The primary α-Al is able to accommodate the stress concentration before the final failure which improves the ductility of the alloy, and the final failure is mainly eutectic separation.

The elongations of the alloys at different temperatures are dominated by the volume fraction of the intermetallic phases and α-Al. There is not much difference in primary intermetallic phases between these two alloys. The near-eutectic alloy A has the lowest elongation, and further introducing ~40% α-Al (Alloy B) is able to improve the elongation from 0.95% to 2%. The yield strength is mainly determined by the volume fraction of the eutectic mixture in these two alloys both at room and elevated temperatures, and a higher volume fraction of the eutectic mixture contributes to a higher yield strength. A383 has the highest EL and lowest YS among the three alloys at room and elevated

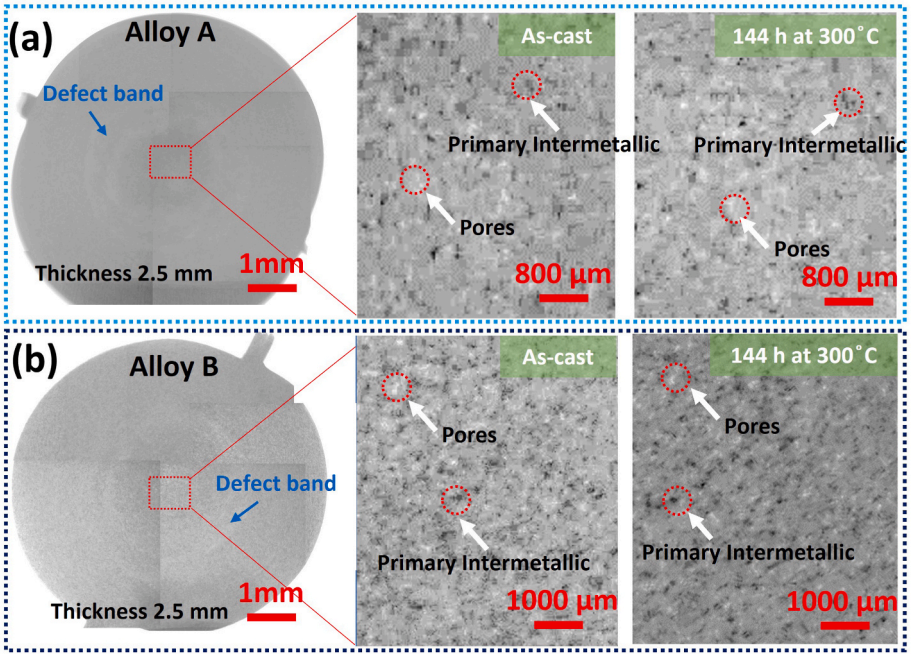

Fig. 14. X-ray micro-CT 2D images showing the porosities in the cross-section of tensile test specimens with a thickness of 2.5 mm under as-cast and after exposure at 300 °C for 144 h; (a) Alloy A, (b) Alloy B.

temperatures, which is mainly because of the lowest volume fraction of intermetallic phases. In addition, the yield strength of Alloy A is only ~14% higher than that of Alloy B at 300 °C, while the area fraction of the eutectic mixture in Alloy B is ~40% lower than that in Alloy A. Obviously, the precipitates in α-Al can be found in Alloy B under as-cast state. Due to the rapid solidification and low solubility of Si, Fe, Ni and Mn, these elements do not have enough time for diffusion to form intermetallic phases at interdendritic regions. Instead, it forms numerous precipitates inside α-Al as shown in Fig. 7. Ni-contained precipitates have high thermal stability and they contain Fe, Ni and Mn elements having very low diffusivity at high temperatures, leading to a less coarsening rate. Thus, it can also make some contributions of strength at 300 °C. The elongation and strength can be balanced by optimisation of the volume fraction of intermetallic phases and α-Al grains. Meanwhile, the introduction of α-Al with supersaturated low diffusivity of elements is an effective way to improve the toughness of the alloy.

Furthermore, the mechanical properties of the alloys in the current work including Alloy A, Alloy B and A383 as well as some other heat-resistant aluminium alloys are summarised in Table 5. Firstly, the EL of Alloy A at room temperature is close to commerical Al–Si near-eutectic alloys such as Al13Si0.6Fe5Cu0.6Mn0.15Ti and Al12Si4Cu2-Ni0.8Mg0.2Nd (wt%) alloys. Secondly, it can be found that these heat-resistant alloys after T6 heat treatment have excellent strength at temperatures below 200 °C, while the strength decreases dramatically at 300 °C. The high strength of the alloys at a temperature below 200 °C results from a high number density of precipitates after T6 heat treatment. However, due to the high diffusivity of Cu and Mg at 300 °C [16], the rapid coarsening of precipitates occurs. Consequently, the contributions of precipitates on strength are greatly mitigated and the strength of these alloys is dominated by the eutectic Si and heat-resistant intermetallic phases. In addition, it can also be found in Table 5 that Alloy A and Alloy B show better combinations of UTS and EL at 300 °C. Especially, Alloy A (near-eutectic) has the highest UTS of 157 ± 6 MPa with good El of 6.5 ± 0.8% at 300 °C. It can be induced that the interconnected network of a large volume fraction of heat-resistant intermetallic phases in Alloy A plays a very important role in the mechanical properties of alloys at high temperatures [19,22,51]. Also, these multicomponent intermetallic phases usually have a higher hardness than their binary or ternary intermetallic phases [48], which may result from enhanced interatomic interactions and chemical bonds.

Fig. 14 (a) and (b) show X-ray micro-CT 2D images before and after thermal exposure at 300 °C for 144 h of Alloy A and Alloy B, respectively. The enlarged micro-CT 2D images before and after thermal exposure are taken from the centre of the sample. From the enlarged micro-CT 2D images, it can be found that some white and black granular particles coexist, which correspond to pores and primary phases respectively. Comparing the same location before and after thermal exposure, it can be found that there is no obvious change in the size and morphology of the pores. It is known that surface blistering and pore expansion after heat treatment at high temperatures (480–540 °C) for a long time can be found in the samples processed by HPDC [33,52–54]. The short time and decreased temperature can diminish pore expansion. Here, the thermal exposure temperature is 300 °C, which is much lower than the solution treatment temperature (480–540 °C). Although the softening of the α-Al matrix takes place at 300 °C, the strength of the α-Al matrix is still high enough to suspend the pore expansion. Hence, the developed die-cast alloys have less sacrifice of mechanical properties serving at elevated temperatures (≤300 °C). Above all, the newly developed alloys processed by HPDC are very potential for industrial application at elevated temperatures.

5. Conclusions

1. Alloy A (78Al15Si4Ni2.5Fe0.5Mn, wt.%) and Alloy B (83.6Al11Si3Ni1.9Fe0.5Mn, wt.%) have been successfully processed by HPDC. Excellent mechanical properties can be achieved in the developed alloys at high temperatures, which is very competitive among heat-resistant aluminium alloys.
2. The as-cast microstructures consist of multicomponent primary intermetallic phases ($Al_{17}(FeNiMn)_4Si$, $Al_4(FeNiMn)Si_2$) and a eutectic mixture in near-eutectic Alloy A. The same multicomponent primary intermetallic phases, the same eutectic mixture and primary α-Al with precipitates can be found in hypoeutectic Alloy B.
3. The melting temperature of the eutectic mixture in Alloy A and Alloy B after HPDC process is 567 °C, and it is a ternary eutectic reaction of

Liquid→α-Al + Si + Al_6(FeNiMn). Al_6(FeNiMn) has a distorted crystal structure of Al_3Ni (a = 6.598 Å, b = 7.352 Å, c = 4.801 Å and α = β = λ = 90°). The eutectic transforms to a quaternary reaction of Liquid→α-Al + Si + Al_3Ni + Al_9(FeNiMn)$_2$ under a slow cooling rate.
4. Al_{17}(FeNiMn)$_4$Si phase shows block-like morphology with a distorted crystal structure of $Al_{5.6}Fe_2$ (a = 7.656 Å, b = 6.415 Å, c = 4.218 Å and α = β = λ = 90°). Al_4(FeNiMn)Si_2 phase shows plate-like morphology with a distorted crystal structure of $FeAl_3Si_2$ (a = b = 6.061 Å, c = 9.525 Å and α = β = λ = 90°). The total volume fractions of primary intermetallic phases are 5.8% in Alloy A and 4.9% in Alloy B.
5. No pore expansion has been observed in these two alloys after thermal exposure at 300 °C for 144 h.

CRediT authorship contribution statement

Qing Cai: Conceptualization, Methodology, Investigation, Writing – original draft, Writing – review & editing. **Ewan Lordan:** Characterisation, Experiment. **Shihao Wang:** Characterisation, Experiment. **Guangyu Liu:** Characterisation, Experiment. **Chamini L. Mendis:** Characterisation, Methodology, Investigation, Writing – review & editing. **Isaac T.H. Chang:** Conceptualization, Writing – review & editing, Supervision. **Shouxun Ji:** Conceptualization, Writing – review & editing, Methodology, Investigation.

Declaration of competing interest

The authors declare that they have no known competing financial interests or personal relationships that could have appeared to influence the work reported in this paper.

Data availability

The authors do not have permission to share data.

Acknowledgements

The authors gratefully acknowledge the support from the Engineering and Physical Sciences Research Council (EPSRC) for the financial support on Future Liquid Metal Engineering (LiME) Hub (EP/N007638/1). The authors would thank Prof Zhongyun Fan, Director of BCAST for the provision of processing and characterisation facilities and Experimental Techniques Centre at Brunel University London for access to the scanning and transmission electron microscopes.

Appendix A. Supplementary data

Supplementary data to this article can be found online at https://doi.org/10.1016/j.msea.2023.144977.

References

[1] M. Tisza, I. Czinege, Comparative study of the application of steels and aluminium in lightweight production of automotive parts, Int. J. Light. Mater. Manuf. 1 (2018) 229–238, https://doi.org/10.1016/j.ijlmm.2018.09.001.
[2] W.S. Miller, L. Zhuang, J. Bottema, A.J. Wittebrood, P. De Smet, A. Haszler, A. Vieregge, Recent development in aluminium alloys for the automotive industry, Mater. Sci. Eng. 280 (2000) 37–49, https://doi.org/10.1016/S0921-5093(99)00653-X.
[3] H. Ye, An overview of the development of Al-Si-alloy based material for engine applications, J. Mater. Eng. Perform. 12 (2003) 288–297, https://doi.org/10.1361/105994903770343132.
[4] M. Di Sabatino, L. Arnberg, Castability of aluminium alloys, Trans. Indian Inst. Met. 2009 624 (62) (2010) 321–325, https://doi.org/10.1007/S12666-009-0049-2.
[5] P. Pandey, S.K. Makineni, B. Gault, K. Chattopadhyay, On the origin of a remarkable increase in the strength and stability of an Al rich Al-Ni eutectic alloy by Zr addition, Acta Mater. 170 (2019) 205–217, https://doi.org/10.1016/j.actamat.2019.03.025.
[6] E.R.R. Wang, X.D.D. Hui, G.L.L. Chen, Eutectic Al-Si-Cu-Fe-Mn alloys with enhanced mechanical properties at room and elevated temperature, Mater. Des. 32 (2011) 4333–4340, https://doi.org/10.1016/j.matdes.2011.04.005.
[7] K. Hu, Q. Xu, X. Ma, Q. Sun, T. Gao, X. Liu, A novel heat-resistant Al–Si–Cu–Ni–Mg base material synergistically strengthened by Ni-rich intermetallics and nano-AlNp microskeletons, J. Mater. Sci. Technol. 35 (2019) 306–312, https://doi.org/10.1016/j.jmst.2018.09.051.
[8] X. Du, T. Gao, G. Liu, X. Liu, In situ synthesizing SiC particles and its strengthening effect on an Al–Si–Cu–Ni–Mg piston alloy, J. Alloys Compd. 695 (2017) 1–8, https://doi.org/10.1016/j.jallcom.2016.10.170.
[9] G. Han, W. Zhang, G. Zhang, Z. Feng, Y. Wang, High-temperature mechanical properties and fracture mechanisms of Al-Si piston alloy reinforced with in situ TiB2 particles, Mater. Sci. Eng. 633 (2015) 161–168, https://doi.org/10.1016/j.msea.2015.03.021.
[10] H. Yi, N. Ma, X. Li, Y. Zhang, H. Wang, High-temperature mechanics properties of in situ TiB2p reinforced Al-Si alloy composites, Mater. Sci. Eng. 419 (2006) 12–17, https://doi.org/10.1016/j.msea.2005.10.020.
[11] H.F. El-Labban, M. Abdelaziz, E.R.I. Mahmoud, Preparation and characterization of squeeze cast-Al–Si piston alloy reinforced by Ni and nano-Al2O3 particles, J. King Saud Univ. - Eng. Sci. 28 (2016) 230–239, https://doi.org/10.1016/j.jksues.2014.04.002.
[12] N.A. Belov, D.G. Eskin, N.N. Avxentieva, Constituent phase diagrams of the Al-Cu-Fe-Mg-Ni-Si system and their application to the analysis of aluminium piston alloys, Acta Mater. 53 (2005) 4709–4722, https://doi.org/10.1016/j.actamat.2005.07.003.
[13] L. Gao, X. Ou, S. Ni, K. Li, Y. Du, M. Song, Effects of θ′ precipitates on the mechanical performance and fracture behavior of an Al–Cu alloy subjected to overaged condition, Mater. Sci. Eng. 762 (2019), 138091, https://doi.org/10.1016/j.msea.2019.138091.
[14] D.G. Eskin, Decomposition of supersaturated solid solutions in Al-Cu-Mg-Si alloys, J. Mater. Sci. 38 (2003) 279–290, https://doi.org/10.1023/A:1021109514892.
[15] M. Yang, H. Chen, A. Orekhov, Q. Lu, X. Lan, K. Li, S. Zhang, M. Song, Y. Kong, D. Schryvers, Y. Du, Quantified contribution of β″ and β′ precipitates to the strengthening of an aged Al–Mg–Si alloy, Mater. Sci. Eng. 774 (2020), 138776, https://doi.org/10.1016/J.MSEA.2019.138776.
[16] Y. Du, Y.A. Chang, B. Huang, W. Gong, Z. Jin, H. Xu, Z. Yuan, Y. Liu, Y. He, F. Y. Xie, Diffusion coefficients of some solutes in fcc and liquid Al: critical evaluation and correlation, Mater. Sci. Eng. 363 (2003) 140–151, https://doi.org/10.1016/S0921-5093(03)00624-5.
[17] A.R. Farkoosh, M. Pekguleryuz, Enhanced mechanical properties of an Al-Si-Cu-Mg alloy at 300°C: effects of Mg and the Q-precipitate phase, Mater. Sci. Eng. 621 (2015) 277–286, https://doi.org/10.1016/j.msea.2014.10.080.
[18] L. Zuo, B. Ye, J. Feng, X. Kong, H. Jiang, W. Ding, Effect of Q-Al5Cu2Mg8Si6 phase on mechanical properties of Al-Si-Cu-Mg alloy at elevated temperature, Mater. Sci. Eng. 693 (2017) 26–32, https://doi.org/10.1016/j.msea.2017.03.087.
[19] K. Bugelnig, F. Sket, H. Germann, T. Steffens, R. Koos, F. Wilde, E. Boller, G. Requena, Influence of 3D connectivity of rigid phases on damage evolution during tensile deformation of an AlSi12Cu4Ni2 piston alloy, Mater. Sci. Eng. 709 (2018) 193–202, https://doi.org/10.1016/j.msea.2017.10.035.
[20] Y. Yang, K. Yu, Y. Li, D. Zhao, X. Liu, Evolution of nickel-rich phases in Al-Si-Cu-Ni-Mg piston alloys with different Cu additions, Mater. Des. 33 (2012) 220–225, https://doi.org/10.1016/j.matdes.2011.06.058.
[21] L. Zuo, B. Ye, J. Feng, H. Zhang, X. Kong, H. Jiang, Effect of ε-Al3Ni phase on mechanical properties of Al–Si–Cu–Mg–Ni alloys at elevated temperature, Mater. Sci. Eng. 772 (2020), 138794, https://doi.org/10.1016/j.msea.2019.138794.
[22] G. Li, H. Liao, X. Suo, Y. Tang, U.S. Dixit, P. Petrov, Cr-induced morphology change of primary Mn-rich phase in Al-Si-Cu-Mn heat resistant aluminum alloys and its contribution to high temperature strength, Mater. Sci. Eng. 709 (2018) 90–96, https://doi.org/10.1016/j.msea.2017.10.049.
[23] T. Gao, X. Zhu, Q. Sun, X. Liu, Morphological evolution of ZrAlSi phase and its impact on the elevated-temperature properties of Al-Si piston alloy, J. Alloys Compd. 567 (2013) 82–88, https://doi.org/10.1016/j.jallcom.2013.03.064.
[24] I. Chang, Q. Cai, From simple binary to complex multicomponent eutectic alloys, Prog. Mater. Sci. 123 (2022), 100779, https://doi.org/10.1016/j.pmatsci.2021.100779.
[25] C.S. Tiwary, P. Pandey, S. Sarkar, R. Das, S. Samal, K. Biswas, K. Chattopadhyay, Five decades of research on the development of eutectic as engineering materials, Prog. Mater. Sci. 123 (2022), 100793, https://doi.org/10.1016/j.pmatsci.2021.100793.
[26] B. Chanda, G. Potnis, P.P. Jana, J. Das, A review on nano-/ultrafine advanced eutectic alloys, J. Alloys Compd. 827 (2020), 154226, https://doi.org/10.1016/j.jallcom.2020.154226.
[27] Y. Kaygisiz, N. Maraşli, Microstructural, mechanical and electrical characterization of directionally solidified Al-Si-Mg eutectic alloy, J. Alloys Compd. 618 (2015) 197–203, https://doi.org/10.1016/j.jallcom.2014.08.056.
[28] U. Böyük, S. Engin, N. Maraşli, Microstructural characterization of unidirectional solidified eutectic Al-Si-Ni alloy, Mater. Char. 62 (2011) 844–851, https://doi.org/10.1016/j.matchar.2011.05.010.
[29] U. Böyük, Physical and mechanical properties of Al-Si-Ni eutectic alloy, Met. Mater. Int. 18 (2012) 933–938, https://doi.org/10.1007/s12540-012-6004-5.
[30] L. Wang, M. Makhlouf, D. Apelian, Aluminium die casting alloys: alloy composition, microstructure, and properties-performance relationships, Int. Mater. Rev. 40 (1995) 221–238, https://doi.org/10.1179/095066095790151133.
[31] R. Molina, P.A.T. Aluminum, M.R. Politecnico, Mechanical characterization of aluminium alloys for high temperature applications Part1: Al-Si-Cu alloys, Metall.

Sci. Tecnol. 29 (2011) 5–15. https://www.fracturae.com/index.php/MST/article/view/1150/1102. (Accessed 24 July 2022).
[32] E. Gariboldi, J.N. Lemke, L. Rovatti, O. Baer, G. Timelli, F. Bonollo, High-temperature behavior of high-pressure diecast alloys based on the Al-Si-Cu system: the role played by chemical composition, Metals 8 (2018), https://doi.org/10.3390/met8050348.
[33] R.N. Lumley, R.G. O'Donnell, D.R. Gunasegaram, M. Givord, Heat treatment of high-pressure die castings, Metall. Mater. Trans. 38 (2007) 2564–2574, https://doi.org/10.1007/s11661-007-9285-4.
[34] S. Seifeddine, D. Poletaeva, M. Ghorbani, A. Jarfors, Heat treating of high pressure die cast components: challenges and possibilities, in: Light Met. 2014, Springer International Publishing, Cham, 2014, pp. 183–188, https://doi.org/10.1002/9781118888438.ch32.
[35] W. Yang, S. Ji, X. Zhou, I. Stone, G. Scamans, G.E. Thompson, Z. Fan, Heterogeneous nucleation of α-Al grain on primary α-AlFeMnSi intermetallic investigated using 3D SEM Ultramicrotomy and HRTEM, Metall. Mater. Trans. 45 (2014) 3971–3980, https://doi.org/10.1007/s11661-014-2346-6.
[36] S. Ji, W. Yang, F. Gao, D. Watson, Z. Fan, Effect of iron on the microstructure and mechanical property of Al–Mg–Si–Mn and Al–Mg–Si diecast alloys, Mater. Sci. Eng. 564 (2013) 130–139, https://doi.org/10.1016/j.msea.2012.11.095.
[37] Q. Cai, C.L. Mendis, I.T.H. Chang, Z. Fan, Microstructure evolution and mechanical properties of new die-cast Al-Si-Mg-Mn alloys, Mater. Des. 187 (2020), 108394, https://doi.org/10.1016/j.matdes.2019.108394.
[38] U. Burkhardt, Y. Grin, M. Ellner, K. Peters, Structure refinement of the iron–aluminium phase with the approximate composition Fe2Al5, Acta Crystallogr. B 50 (1994) 313–316, https://doi.org/10.1107/S0108768193013989.
[39] M. Cooper, The crystal structure of the ternary alloy α(AlFeSi), Acta Crystallogr. 23 (1967) 1106–1107, https://doi.org/10.1107/s0365110x67004372.
[40] C. Gueneau, C. Servant, F. D'Yvoire, N. Rodier, FeAl3Si2, Acta Crystallogr. Sect. C Cryst. Struct. Commun. 51 (1995) 177–179, https://doi.org/10.1107/S0108270194009030.
[41] Z. Bian, Y. Liu, S. Dai, Z. Chen, M. Wang, D. Chen, H. Wang, Regulating microstructures and mechanical properties of Al–Fe–Ni alloys, Prog. Nat. Sci. Mater. Int. 30 (2020) 54–62, https://doi.org/10.1016/j.pnsc.2019.12.006.
[42] M. Warmuzek, Chemical composition of the Ni-containing intermetallic phases in the multicomponent Al alloys, J. Alloys Compd. 604 (2014) 245–252, https://doi.org/10.1016/j.jallcom.2014.03.119.
[43] B. Cantor, Multicomponent high-entropy Cantor alloys, Prog. Mater. Sci. 120 (2021), 100754, https://doi.org/10.1016/j.pmatsci.2020.100754.
[44] Y.F. Ye, Q. Wang, J. Lu, C.T. Liu, Y. Yang, The generalized thermodynamic rule for phase selection in multicomponent alloys, Intermetallics 59 (2015) 75–80, https://doi.org/10.1016/j.intermet.2014.12.011.
[45] N. Zhou, S. Jiang, T. Huang, M. Qin, T. Hu, J. Luo, Single-phase high-entropy intermetallic compounds (HEICs): bridging high-entropy alloys and ceramics, Sci. Bull. 64 (2019) 856–864, https://doi.org/10.1016/j.scib.2019.05.007.
[46] H. Huang, Y. Sun, P. Cao, Y. Wu, X. Liu, S. Jiang, H. Wang, Z. Lu, On cooling rates dependence of microstructure and mechanical properties of refractory high-entropy alloys HfTaTiZr and HfNbTiZr, Scripta Mater. 211 (2022), 114506, https://doi.org/10.1016/j.scriptamat.2022.114506.
[47] T.H. Chou, J.C. Huang, C.H. Yang, S.K. Lin, T.G. Nieh, Consideration of kinetics on intermetallics formation in solid-solution high entropy alloys, Acta Mater. 195 (2020) 71–80, https://doi.org/10.1016/j.actamat.2020.05.015.
[48] M. Tupaj, A.W. Orłowicz, M. Mróz, A. Trytek, A.J. Dolata, A. Dziedzic, A study on material properties of intermetallic phases in a multicomponent hypereutectic al-si alloy with the use of nanoindentation testing, Materials 13 (2020) 1–17, https://doi.org/10.3390/ma13245612.
[49] C.L. Chen, R.C. Thomson, The combined use of EBSD and EDX analyses for the identification of complex intermetallic phases in multicomponent Al-Si piston alloys, J. Alloys Compd. 490 (2010) 293–300, https://doi.org/10.1016/j.jallcom.2009.09.181.
[50] M.S. Jo, Y.H. Cho, J.M. Lee, S.H. Kim, J.Y. Kang, J.G. Jung, S.B. Kim, J. il Jang, A new Zr-rich intermetallic phase in an Al-14Si-3Cu-4.5Ni casting alloy with trace additions of Zr, Intermetallics 117 (2020), 106667, https://doi.org/10.1016/j.intermet.2019.106667.
[51] X. Suo, H. Liao, Y. Hu, U.S. Dixit, P. Petrov, formation of Al15Mn3Si2 phase during solidification of a novel Al-12%Si-4%Cu-1.2%Mn heat-resistant alloy and its thermal stability, J. Mater. Eng. Perform. 27 (2018) 2910–2920, https://doi.org/10.1007/s11665-018-3133-0.
[52] X. Dong, H. Yang, X. Zhu, S. Ji, High strength and ductility aluminium alloy processed by high pressure die casting, J. Alloys Compd. 773 (2019) 86–96, https://doi.org/10.1016/j.jallcom.2018.09.260.
[53] O. Trudonoshyn, P. Randelzhofer, C. V, Heat treatment of high-pressure die casting Al-Mg-Si-Mn-Zn alloys, J. Alloys Compd. 872 (2021), 159692, https://doi.org/10.1016/j.jallcom.2021.159692.
[54] Q. Cai, C.L. Mendis, I.T.H. Chang, Z. Fan, Effect of short T6 heat treatment on the microstructure and the mechanical properties of newly developed die-cast Al–Si–Mg–Mn alloys, Mater. Sci. Eng. 788 (2020), 139610, https://doi.org/10.1016/j.msea.2020.139610.
[55] Y. Sui, D. Ji, L. Han, Q. Wang, Characterization of the aging precipitates of Al-12Si-4Cu-2Ni-0.8Mg-0.2Gd piston alloy, JOM (J. Occup. Med.) 71 (2019) 366–372, https://doi.org/10.1007/s11837-018-3080-0.
[56] L. Han, Y. Sui, Q. Wang, K. Wang, Y. Jiang, Effects of Nd on microstructure and mechanical properties of cast Al-Si-Cu-Ni-Mg piston alloys, J. Alloys Compd. 695 (2017) 1566–1572, https://doi.org/10.1016/j.jallcom.2016.10.300.
[57] H. Li, B. Lin, R. Xu, K. Liu, H. Xiao, Y. Zhao, Enhanced mechanical properties of Al–Si–Cu–Mn–Fe alloys at elevated temperatures through grain refinement and dispersoid strengthening, Mater. Sci. Technol. 36 (2020) 307–319, https://doi.org/10.1080/02670836.2019.1705039.
[58] K. Yu, W. Li, S. Li, J. Zhao, Mechanical properties and microstructure of aluminum alloy 2618 with Al3(Sc. Zr) phases, Mater. Sci. Eng. 368 (2004) 88–93, https://doi.org/10.1016/j.msea.2003.09.092.